

Experimental upper limits on branching fractions for unexpected decay modes of the τ lepton

K. G. Hayes,* M. L. Perl, M. S. Alam,[†] A. M. Boyarski, M. Breidenbach, D. L. Burke,
J. Dorenbosch,* J. M. Dorfan, G. J. Feldman, M. E. B. Franklin, G. Hanson, T. Himel,*
D. G. Hitlin,[‡] R. J. Hollebeek, W. R. Innes, J. A. Jaros, P. Jenni,* R. R. Larsen,
V. Lüth, B. Richter, A. Roussarie,[¶] D. L. Scharre, R. H. Schindler,*
R. F. Schwitters,[§] J. L. Siegrist, H. Taureg,* M. Tonutti,^{||} R. A. Vidal,
J. M. Weiss, and H. Zaccane,^{¶¶}

Stanford Linear Accelerator Center, Stanford University, Stanford, California 94305

G. S. Abrams, C. A. Blocker, A. Blondel, W. C. Carithers, W. Chinowsky, M. W. Coles,**
S. Cooper,** W. E. Dieterle, J. B. Dillon, M. W. Eaton, G. Gidal, G. Goldhaber,
A. D. Johnson, J. A. Kadyk, A. J. Lankford, M. Levi,[§] R. E. Millikan, M. E. Nelson,
C. Y. Pang, J. F. Patrick, J. Strait, G. H. Trilling, E. N. Vella, and I. Videau

Lawrence Berkeley Laboratory and Department of Physics, University of California, Berkeley, California 94720

(Received 1 February 1982)

Searches for 12 neutrinoless decay modes of the τ which violate lepton-number conservation have been made using the reaction $e^+e^- \rightarrow \tau^+\tau^-$. No evidence for lepton-number violation is observed, and we have set upper limits (90% C.L.) on the branching ratio for each decay mode. The branching-ratio limits on the radiative decays $\tau \rightarrow \mu\gamma$ and $\tau \rightarrow e\gamma$ are 0.055 and 0.064%, respectively. For the charged lepton decays $\tau \rightarrow eee$, $\tau \rightarrow e\mu\mu$, $\tau \rightarrow \mu ee$, and $\tau \rightarrow \mu\mu\mu$, the branching ratio limits are 0.040, 0.033, 0.044, and 0.049%, respectively. Upper limits on the branching ratios for the following charged lepton + neutral hadron decays are $\tau \rightarrow e\rho^0$ (0.037%), $\tau \rightarrow \mu\rho^0$ (0.044%), $\tau \rightarrow eK^0$ (0.13%), $\tau \rightarrow \mu K^0$ (0.10%), $\tau \rightarrow e\pi^0$ (0.21%), and $\tau \rightarrow \mu\pi^0$ (0.082%). We also use these data to search for the pair production in e^+e^- annihilation of some unconventional particles with masses less than about $3 \text{ GeV}/c^2$.

I. INTRODUCTION

This paper describes a search for decay modes of the τ lepton which do not contain the τ neutrino (ν_τ). We did not find these modes, and we report upper limits on the branching fractions. The absence of such modes is consistent with our current model of the τ , which states that the τ^- and ν_τ have a unique conserved lepton number.

This search was carried out using the τ -production reaction

$$e^+ + e^- \rightarrow \tau^+ + \tau^- \quad (1)$$

at the SPEAR electron-positron colliding-beams facility of the Stanford Linear Accelerator Center. The Mark II magnetic detector was used to acquire about 17000 nb^{-1} of data in the center-of-mass energy range of $3.85 \leq E_{\text{c.m.}} \leq 6.85 \text{ GeV}$.

We also use these data to search for the pair production of unconventional particles with masses

less than about $3 \text{ GeV}/c^2$ which might be produced in e^+e^- annihilation. For example, we searched for an excited electron e^* with the decay mode $e^* \rightarrow e + \gamma$.

The theory associated with the nature and decay properties of the τ has been discussed in detail in many papers¹⁻⁴; and there is no need to review that material here. This is particularly true because the τ behaves so simply. All recent published experimental studies of the production and decay properties of the τ agree^{1,2} with the following model: (a) The τ is a spin- $\frac{1}{2}$ point particle obeying the Dirac equation. (b) The τ^- and its associated neutrino ν_τ have a unique, conserved, lepton number. (c) The τ decays only through the weak interaction with $V-A$ coupling. According to this model all decays of the τ have the form

$$\tau^- \rightarrow \nu_\tau + a + b + \cdots, \quad (2)$$

and decay modes which do not contain the ν_τ

violate this model.

We have searched for three types of model-violating decay modes:

Radiative modes:

$$\begin{aligned}\tau^- &\rightarrow e^- + \gamma, \\ \tau^- &\rightarrow \mu^- + \gamma.\end{aligned}\quad (3)$$

Three-lepton modes:

$$\begin{aligned}\tau^- &\rightarrow e^- + e^+ + e^-, \\ \tau^- &\rightarrow \mu^- + e^+ + e^-, \\ \tau^- &\rightarrow e^- + \mu^+ + \mu^-, \\ \tau^- &\rightarrow \mu^- + \mu^+ + \mu^-.\end{aligned}\quad (4)$$

Neutral-hadron decay modes:

$$\begin{aligned}\tau^- &\rightarrow e^- + \pi^0, \\ \tau^- &\rightarrow \mu^- + \pi^0, \\ \tau^- &\rightarrow e^- + K^0, \\ \tau^- &\rightarrow \mu^- + K^0, \\ \tau^- &\rightarrow e^- + \rho^0, \\ \tau^- &\rightarrow \mu^- + \rho^0.\end{aligned}\quad (5)$$

Note that for brevity, when we describe a decay mode using the τ^- we also include the charge-conjugate decay mode of the τ^+ . Thus a search for $\tau^- \rightarrow e^- + \gamma$ includes a search for $\tau^+ \rightarrow e^+ + \gamma$.

This paper is limited to a presentation of our experimental results. We shall not attempt to discuss the detailed limitations these results put on the various possible modifications of the conventional theory of the τ . Some of these limitations have been described by Hayes.⁵

The plan of this paper is as follows. The apparatus, data acquisition, and general search method are described in Secs. II and III. Sections IV, V, and VI present the search method and results for the types of decay modes listed in Eqs. (3), (4), and (5), respectively. Finally, in Sec. VII we describe the search for unconventional particles using this data, and we summarize the null results.

II. APPARATUS AND DATA ACQUISITION

Figures 1 and 2 show cross-sectional and isometric views of the Mark II magnetic detector. As a particle leaves the interaction region it passes through the beam pipe, and then through a set of cylindrical scintillation counters, called the pipe

counters. The particle then enters the cylindrical drift chamber.

This drift chamber,⁶ with inner and outer radii of 0.41 and 1.45 m, respectively, is immersed in a longitudinal, solenoidal, 0.4-T magnetic field. Charged particles are detected in over 80% of the solid angle. The chamber has 16 layers; 6 are parallel to the beam axis, and the other 10 are rotated by about $\pm 3^\circ$ to determine the momentum component along the beam axis. The average momentum resolution is

$$\Delta p/p = 0.01[(1.5)^2 + p^2]^{1/2}, \quad (6)$$

where the constant term represents the effects of multiple Coulomb scattering, and the momentum-dependent term accounts for the 200- μm single-cell resolution. Here p is the momentum in GeV/c.

The time-of-flight scintillation counters are located between the drift chamber's outer cover and the solenoid coil, at a 1.5-m radius from the beam axis. The scintillator is viewed at both ends to give a time resolution of 300 psec. This allows separation of electrons from pions below 300 MeV/c, kaons from pions below 1.3 GeV/c, and protons from pions below 2.0 GeV/c.

The lead and liquid-argon electromagnetic shower detector lies just outside the magnet coil. Eight modules completely surround the detector in azimuth and cover 60% of the total solid angle. The detector consists of 37 2-mm-thick lead plates separated by 3-mm gaps filled with liquid argon. The total number of radiation lengths in the detec-

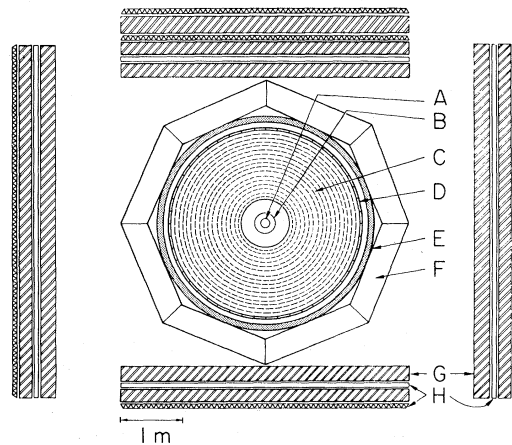


FIG. 1. Cross-sectional view of the Mark II detector. (A) vacuum chamber, (B) pipe counter, (C) 16-layer drift chamber, (D) time-of-flight counters, (E) solenoid coil, (F) lead—liquid-argon shower detectors, (G) iron flux return and hadron absorber, (H) muon proportional tubes.

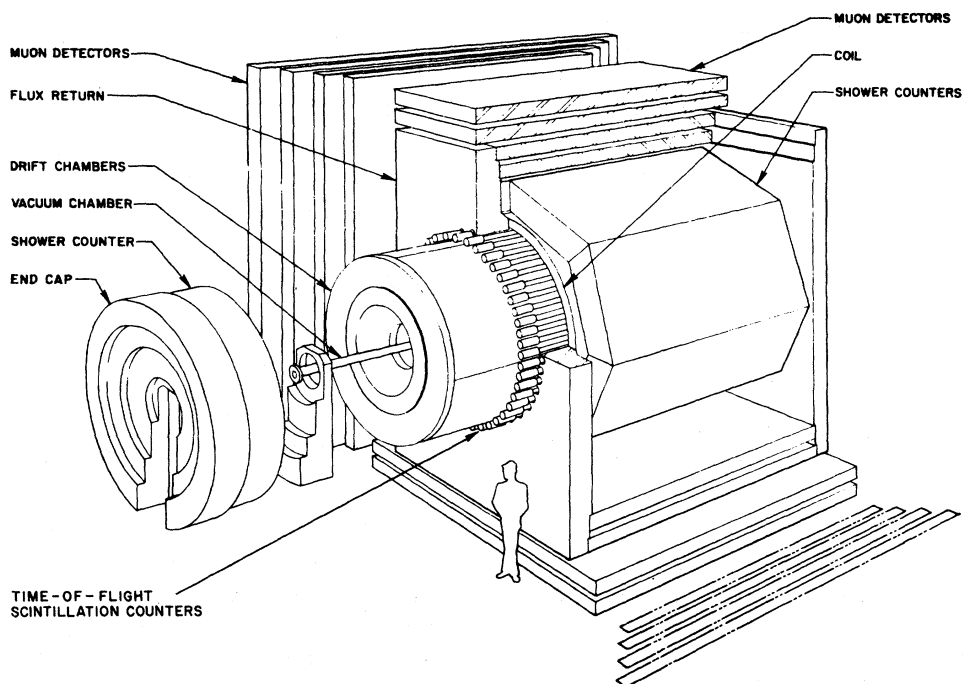


FIG. 2. Isometric-projection view of the Mark II detector.

tor is 14. The lead plates are alternately continuous ground planes and ionization signal collecting high-voltage planes. The latter are divided into strips which provide spatial information. The electromagnetic energy resolution is

$$\Delta E/E = 0.13/[E (\text{GeV})]^{1/2}. \quad (7)$$

Electrons are separated from hadrons and muons using the properties of the electromagnetic shower. The principal properties used are the ratio of the shower energy to the momentum of the particle, and the ratio of the energies deposited in the front and back of the module. The actual algorithm is quite complicated and is discussed in Refs. 5 and 7. Table I gives the probability of misidentifying a π^\pm as an e^\pm using the shower detector and time-of-flight counter information.

The photon-detection efficiency, Fig. 3, was measured using constrained fits to the processes $\psi \rightarrow \pi^+ \pi^- \pi^0$ and $\psi \rightarrow 2\pi^+ 2\pi^- \pi^0$. Upward fluctuations in the electronic noise can cause false photons to be found by the photon-detection software. The threshold in the efficiency is caused by the cuts required to keep the spurious photon rate acceptable.

The muon-identification system, which lies outside the liquid-argon shower detectors, consists of several layers of thick steel plates and proportional tubes (Figs. 1 and 2). Before a particle can reach

the first plate, it must traverse inner-detector material, the magnet coil, and the shower detector, equivalent to 20 cm of iron. The steel absorbing plates are 23 cm thick in the first two layers and 30 cm thick in the third layer of the top wall. The first layer is located approximately 3 m from the interaction region, and subtends 51% of the solid angle, while the second layer is approximately of equal area and covers 90% of the solid angle sub-

TABLE I. The probability $P(\pi^\pm \rightarrow e)$ of a π^\pm being called an e^\pm and the probability $P(e^\pm \rightarrow e)$ of an e^\pm being correctly identified using the liquid-argon electromagnetic shower detector and the time-of-flight counters.

Momentum (GeV/c)	$P(\pi^\pm \rightarrow e)$	$P(e^\pm \rightarrow e)$
0.3–0.4	0.098 ± 0.007	0.730 ± 0.007
0.4–0.5	0.111 ± 0.007	0.760 ± 0.009
0.5–0.6	0.069 ± 0.006	0.833 ± 0.011
0.6–0.7	0.056 ± 0.006	0.866 ± 0.012
0.7–0.8	0.032 ± 0.006	0.823 ± 0.017
0.8–0.9	0.052 ± 0.009	0.857 ± 0.018
0.9–1.1	0.031 ± 0.002	0.848 ± 0.015
1.1–1.3	0.036 ± 0.004	0.918 ± 0.015
1.3–1.5	0.056 ± 0.010	0.968 ± 0.008

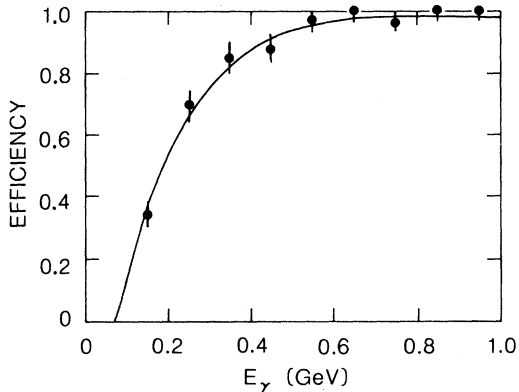


FIG. 3. Measured efficiency for photon detection of the liquid-argon shower detector. The curve is a Monte Carlo calculation of that efficiency.

tended by the first. The top wall's third layer subtends 9% of the total solid angle. The momentum of a muon must exceed about 700 MeV/c to penetrate the first layer.

Behind each absorbing plate there is a plane of proportional tubes which run the full width of the wall and which measure one of the two orthogonal coordinates. The tubes are oriented so that the second and third layers measure the coordinate orthogonal to that measured by the first. The 1672 tubes used in the system are actually built in the form of eight-tube modules made of extruded aluminum (Fig. 4). The ability of this system to separate hadrons from muons is discussed in Ref. 5. An illustration of that ability is given in Fig. 5.

Data were acquired using a two-level system⁸ composed of a fast (500 nsec) primary trigger whose output sets off a more sophisticated but slower (30 μ sec) secondary trigger. The primary trigger demands the coincidence of a beam-crossing signal from a pickup electrode with the pipe counter, and hits in at least four of nine selected drift-chamber layers. The pipe counter limits the cosmic-ray background to tracks which pass within 12 cm of the beam axis. The loose requirement on the drift-chamber data results in near perfect effi-

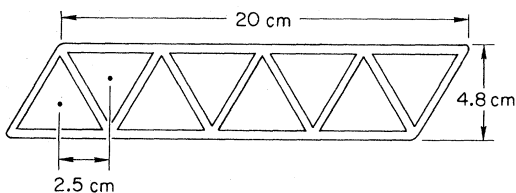


FIG. 4. Cross-sectional view of a muon-system proportional-tube module containing eight tubes.

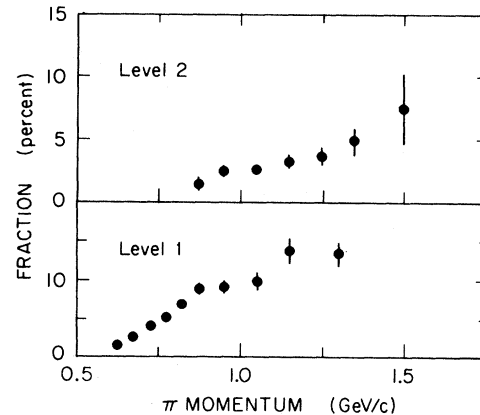


FIG. 5. Probability in percent of a pion being misidentified as a muon.

ciency for tracks which pass through all of the drift-chamber layers.

The secondary trigger is an electronic track finder and track counter. It works by rotating crescent-shaped masks axially around the drift chamber and defining tracks if a minimum number of layers have hits within the mask boundaries. Twenty-four masks are used, allowing tracks of different momenta and charge to be recognized. The criterion used for most of the experiment was at least one track with four out of six axial layers hit, and one track with at least three hits in the five innermost layers. This resulted in a trigger rate of a few Hz. The combination drift-chamber and trigger-logic system worked so well that the trigger efficiency for event topologies used in this analysis (that is, tracks which enter the shower detector or muon system solid angle) is nearly 100%.

The data listed in Table II were used in this analysis. We give for each energy interval the integrated luminosity and the number of produced τ

TABLE II. τ pair production vs center-of-mass energy.

Interval (GeV)	Integrated luminosity (nb ⁻¹)	Number of produced $\tau^+\tau^-$ pairs
3.85—4.25	2129	7348
4.25—4.65	1788	6248
4.65—5.05	1866	6006
5.05—5.45	6176	18136
5.45—6.35	1221	2922
6.35—6.85	3783	7448
Total	16 963	48 108

pairs, the latter being calculated from the luminosity and the τ cross section.¹ The systematic error in the luminosity is estimated to be 6%.

III. GENERAL SEARCH METHOD

We searched for unexpected decay modes by requiring that one of the τ 's in

$$e^+ + e^- \rightarrow \tau^+ + \tau^- \quad (8a)$$

decay into one of the known *single-charged-prong* decay modes. The single-charged-prong decay modes are mainly

$$\tau^+ \rightarrow e^+ + \nu_e + \bar{\nu}_\tau$$

or

$$\tau^+ \rightarrow \mu^+ + \nu_\mu + \bar{\nu}_\tau$$

or

$$\tau^+ \rightarrow \pi^+ + \bar{\nu}_\tau \quad (8b)$$

or

$$\tau^+ \rightarrow \rho^+ + \bar{\nu}_\tau \rightarrow \pi^+ + \gamma + \gamma + \bar{\nu}_\tau .$$

The other τ could then decay unconventionally, such as

$$\tau^- \rightarrow e^- + \gamma$$

or

$$\tau^- \rightarrow \mu^- + \gamma$$

or

$$\tau^- \rightarrow e^- + e^+ + e^- \quad (8c)$$

or

$$\tau^- \rightarrow e^- + \rho^0 \rightarrow e^- + \pi^+ + \pi^- ,$$

and so forth. Of course, the roles of the τ^+ and τ^- could be reversed.

This basic signature in a perfect detector leads to events with two or four charged particles with total charge zero, and with up to two photons. To satisfy this signature in our detector we selected events with the following properties: (a) two, three, or four charged tracks; (b) total charge = 0 for two- or four-track events; (c) total charge = ± 1 for three-track events; (d) any number of photons; and (e) the two-charged-track events have an acoplanarity angle⁹ greater than 5° . The sample containing a total of three charged tracks allowed us to use events in which the three charged parti-

cles in an unconventional decay such as $e^- + e^+ + e^-$ were detected, but the track from the conventional decay was not detected. The acoplanarity requirement eliminates background from $e^+e^- \rightarrow e^+e^-, \mu^+\mu^-$.

IV. SEARCH FOR THE RADIATIVE DECAY MODES $\tau^- \rightarrow e^- \gamma, \mu^- \gamma$

In this search we use two-track, total-charge-zero events with one or more photons:

$$e^+ + e^- \rightarrow l^\pm + x^\pm + \text{one or more } \gamma\text{'s} . \quad (9)$$

Here l means e or μ ; x means e, μ , or hadron.

To reduce the contamination from beam-pipe or beam-gas events, the reconstructed vertex of the two charged prongs must lie within a cylinder 16 cm long with a 4-cm radius centered around the interaction region. To eliminate mismeasured tracks, the vertex-finding algorithm must use both tracks, and the χ^2 from the vertex fit must be less than 100. A minimum-momentum cut of 100 MeV/c is applied to the charged tracks to ensure a well defined cutoff in the detector's response to low-momentum tracks.

The invariant mass m of the photon-lepton system in Eq. (9) is

$$m = [m_l^2 + 2E_\gamma(E_l - p_l \cos\theta)]^{1/2} . \quad (10)$$

Here E_l and p_l are the energy and momentum of the lepton, E_γ is the energy of the photon, and θ is the angle between the photon and lepton. The resolution in this measurement is dominated by the relatively poor photon energy resolution. Since the τ is pair produced, the sum of the energies of its decay products equals the beam energy, and this constraint can be used to improve the resolution of the invariant-mass measurement.

The proper realization of the beam constraint adjusts both the measured photon and lepton energies depending on their relative measurement errors, but in practice is nearly identical to the simple replacement of the photon energy with

$$E_{\gamma, \text{used}} = E_{\text{beam}} - E_l . \quad (11)$$

Figure 6 shows the μ - γ mass resolution as a function of $x = E_l/E_{\text{beam}}$ for three beam energies. If the correct constraint procedure is applied, the resolution levels off as x approaches 1 at a value reflecting the photon energy resolution, but it is so poor that this kinematical region is useless. Conse-

quently we require

$$x \leq 0.77. \quad (12)$$

In the allowed x region, the error in the predicted photon energy is small relative to the error in the photon energy measurement. Therefore, a cut on the χ^2 of the one-constraint (1C) fit is equivalent to a cut on the photon-energy-resolution variable

$$D = (E_{\gamma, \text{used}} - E_{\gamma}) / E_{\gamma, \text{used}}.$$

This variable is normally distributed with a σ of $0.13/[E_{\gamma, \text{used}} (\text{GeV})]^{1/2}$ according to a Monte Carlo study. Hence

$$Z = D(E_{\gamma, \text{used}})^{1/2}$$

is normally distributed with a σ of $0.13 \text{ GeV}^{1/2}$. We eliminate events with large $(E_{\gamma, \text{used}} - E_{\gamma})$ by requiring

$$|Z| \leq 0.20 \text{ GeV}^{1/2}. \quad (13)$$

Figure 7 shows the mass spectra using the entire data sample with the restrictions of Eqs. (12) and (13). Recall that we have also required that the acoplanarity angle be greater than 5° .

These spectra contain background events from conventional electromagnetic reactions such as

$$\begin{aligned} e^+ + e^- &\rightarrow e^+ + e^- + \gamma, \\ e^+ + e^- &\rightarrow e^+ + e^- + \gamma + \gamma, \\ e^+ + e^- &\rightarrow \mu^+ + \mu^- + \gamma, \\ e^+ + e^- &\rightarrow \mu^+ + \mu^- + \gamma + \gamma. \end{aligned} \quad (14)$$

We reduce these backgrounds by a set of constraints discussed in detail in Ref. 5. We shall list these constraints here.

(a) The event must not conserve three-momen-

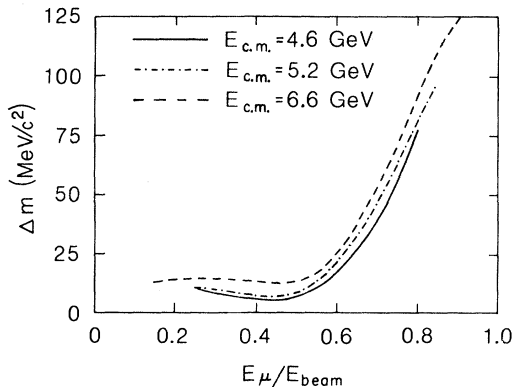


FIG. 6. The μ - γ mass resolution as a function of E_{μ}/E_{beam} .

tum using just the l , x , and γ 's in Eq. (9).

(b) The event must not be consistent with having an undetected photon along the beam direction of greater than 300 MeV energy.

These two constraints remove 65% of the μ - γ candidates and 45% of the e - γ candidates. A small additional fraction of candidates are removed by the following.

(c) The cosine of the angle between the photon and the l - x plane must be less than 0.998.

(d) The cosine of the angle between the photon and either the l or the x must be less than 0.986.

(e) The γ must not reconstruct with another γ in the event to the π^0 mass.

Two additional restrictions are made on the e - γ candidates because of the larger contamination from the reactions in Eq. (14).

(f) The acoplanarity angle⁹ must be greater than 28° .

(g) The x^\pm in Eq. (9) cannot be an identified e^\pm .

The effect of constraints (a)–(g) on the acceptance is shown in Fig. 8. We see that the e - γ acceptance is reduced more than the μ - γ acceptance because of restrictions (f) and (g). The acceptance is calculated using a Monte Carlo method.

With the addition of the cuts discussed above, we obtain the μ - γ invariant-mass spectrum shown in Fig. 9(b). The spectrum in the region near the τ mass is shown with an expanded function scale in Fig. 10(b) along with the resolution function obtained with the Monte Carlo method.

There is no evidence for the $\mu + \gamma$ radiative decay of the τ . Using the measured luminosity and calculated acceptance, we can determine a 90%-confidence-level upper limit to the branching fraction

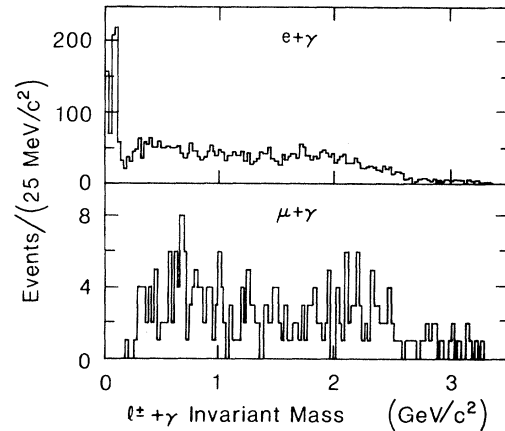


FIG. 7. The l - γ invariant-mass distributions before the application of background-removing constraints.

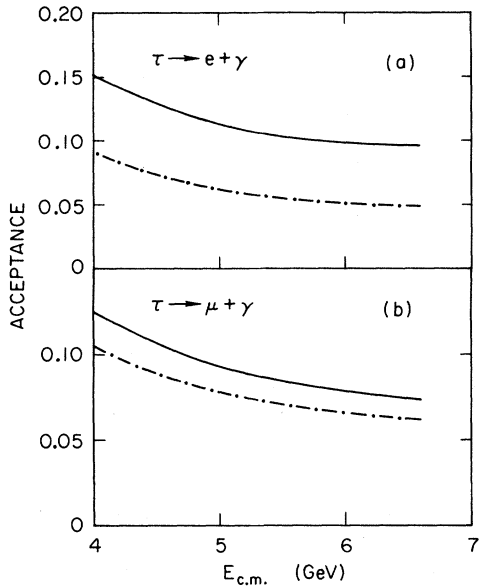


FIG. 8. The acceptance for detecting (a) $\tau \rightarrow e + \gamma$ and (b) $\tau \rightarrow \mu + \gamma$. The solid and dash-dot curves are before and after the application of background-removing constraints.

$$B \leq \lambda(N_{\text{obs}}) / \left[2 \sum_E \sigma(E) L(E) A(E) \right].$$

Here $\lambda(N)$ is the average value for a Poisson distribution such that there is a 90% probability that N_{obs} comes from a distribution with that average value or smaller. Here N_{obs} is the number of events observed within the mass acceptance region, σ is the $e^+e^- \rightarrow \tau^+\tau^-$ cross section, L is the luminosity, A is the acceptance, and E is the center-of-mass energy. The mean acceptance is 7.3%, averaged over the center-of-mass energy range with a weight function proportional to the number of produced τ pairs. Given that the data sample contains 96 000 produced τ leptons, the single event which lies within the 68-MeV/ c^2 -wide region used to define the acceptance determines the 90% confidence level on the branching ratio of the radiative decay $\tau \rightarrow \mu + \gamma$ to be 0.055%.

The $e\text{-}\gamma$ mass spectrum is shown in Figs. 9(a) and 10(a). There is no evidence for the $e + \gamma$ radiative decay of the τ . The one event in Fig. 10(a) within the 68-MeV/ c^2 acceptance interval leads to a 90%-confidence-level upper limit on the branching fraction for the decay $\tau \rightarrow e + \gamma$ of 0.064%.

In looking at Fig. 10, one notices quickly the collection of mass pairs in both $e\gamma$ and $\mu\gamma$ at about 1730 MeV/ c^2 . The immediate question is, "Have we made an error in the mass scale of about 50

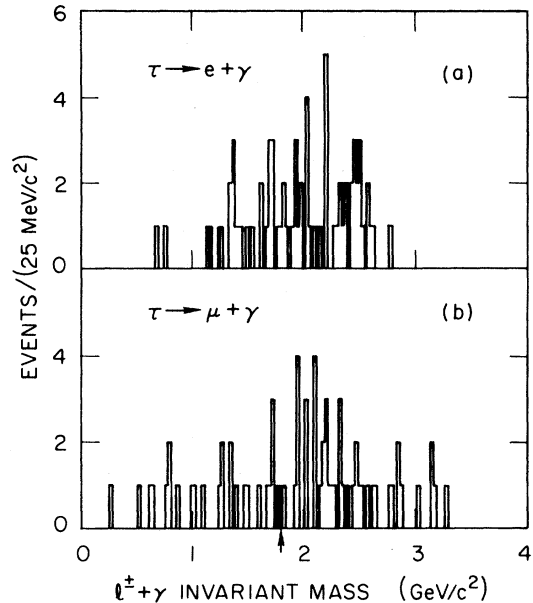


FIG. 9. The $l\text{-}\gamma$ invariant-mass distributions after the application of background-removing constraints. The arrow indicates the position of the τ mass 1.782 GeV/ c^2 .

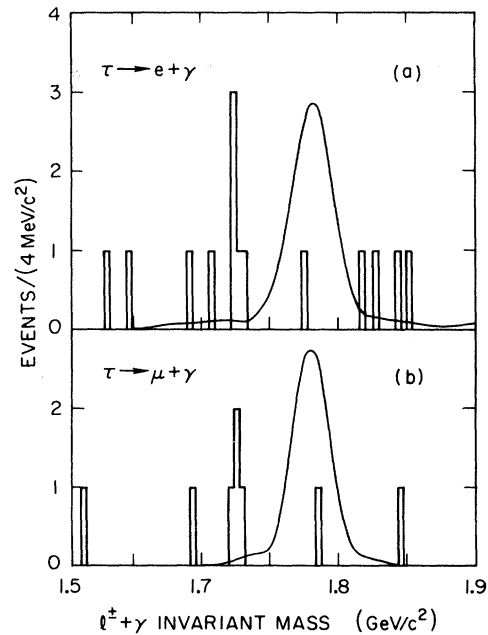


FIG. 10. The $l\text{-}\gamma$ invariant-mass distributions in the neighborhood of the τ mass after the application of background-removing constraints. The mass-resolution-function curve is centered on the τ mass of 1.782 GeV/ c^2 .

MeV/c² so that these mass pairs are from the $e\gamma$ or $\mu\gamma$ decay of the τ ?" We have examined this possibility by studying the possible systematic errors in the three quantities which determine the invariant mass, the beam energy E_{beam} , the lepton energy E_l , and the angle between the lepton and photon θ . Recall that we use the beam-constrained invariant mass so that the relatively poorly measured photon energy has little effect. As indicated by Eq. (11) we essentially use

$$m = [m_l^2 + 2(E_{\text{beam}} - E_l)(E_l - p_l \cos\theta)]^{1/2} . \quad (15)$$

The center of a beam-constrained invariant-mass resolution function depends upon the two very well measured quantities E_{beam} and θ , Eq. (15). Because of the way E_l enters Eq. (15) and since E_l has a flat spectrum for two-body decays, errors in E_l broaden the resolution function, but do not shift the center appreciably. Hence any shift in the mass scale must come from systematic errors in E_b and θ . We have estimated these systematic errors and our upper limit on a mass-scale shift is 12 MeV/c. Hence the $e\gamma$ and $\mu\gamma$ pairs in the vicinity of 1730 MeV/c² in Fig. 10 do not come from decays of the τ . We return to these pairs in Sec. VII B.

V. SEARCH FOR THE THREE-LEPTON DECAY MODES $\tau \rightarrow e^-e^+e^-$, $e^-\mu^+\mu^-$, $\mu^-e^+e^-$, $\mu^-\mu^+\mu^-$

About 70% of τ decays have one charged particle in the decay products. Therefore, in the search for the three-charged-lepton decays of the τ , we use all three- and four-charged-prong events which have a total charge between -1 and 1 , and which have one or more tracks identified as an electron or muon. No restrictions are placed on the number of neutral particles in the event. At least three of the charged tracks must form a vertex located within a cylinder 16 cm long and 4 cm in radius centered about the interaction region. To ensure a well-defined momentum cutoff, all tracks used in any invariant-mass calculation must have a momentum larger than 100 MeV/c and must originate in the event vertex.

The Mark II's acceptance to detect and identify all three leptons from any of the four τ decays listed in Eq. (4) is small and decreases as the number of muons in the decay increases. Thus, we are forced to also consider three-charged-track combinations where only one or two tracks are identi-

fied as leptons. The background from random combinations increases with the number of unidentified tracks. Therefore, the contribution to each of the four decays from combinations where one, two, or three leptons are identified, are accumulated separately so that those with the worst background can be discarded. For example, contributions to the invariant-mass distribution for the decay $\tau \rightarrow e\mu^+\mu^-$ can be from any of the following lepton combinations:

$$exx, \mu xx, e\mu x, x\mu\mu, e\mu\mu, \quad (16)$$

where x represents a particle which was not identified as a lepton. Note that the electric charges of the particles are relevant. The combination exx can contribute to the decay only if x_1 and x_2 have opposite charges. If in the combination μxx both x_1 and x_2 have the opposite charge from the muon, we will consider both cases, where either x_1 or x_2 is assigned the electron mass, and use only the combination which has the best χ^2 for the beam-constrained fit.

Given the measured three-momentum and a mass hypothesis for each charged track, the invariant mass of the three-charged-track combination is

$$m = \left[\left(\sum_i E_i \right)^2 - \left(\sum_i P_i \right)^2 \right]^{1/2} . \quad (17)$$

The resolution in this measurement depends on the center-of-mass energy and the number of electrons in the decay. For the three-muon decay, the resolution is typically 20 to 30 MeV/c², but it is several times worse for the eee decay. This can be improved by a factor of 2 to 3 if the fact that the τ is produced with the beam energy is used to correct the measured track momenta. We define

$$\Delta E = E_{\text{beam}} - \sum_i E_i \quad (18)$$

and

$$Z = \sum_i E_i / E_{\text{beam}} . \quad (19)$$

Obviously we want ΔE to be small and so we set the following requirements on Z :

$$\begin{aligned} A < Z < 1.03 , \\ A(\mu\mu\mu) &= 0.97 , \\ A(e\mu\mu) &= 0.96 = A(\mu ee) , \\ A(eee) &= 0.95 . \end{aligned} \quad (20)$$

All candidates which pass this Z requirement are

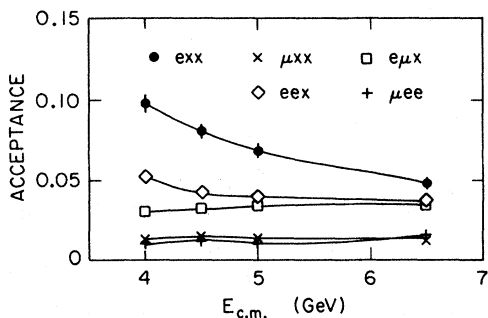


FIG. 11. Acceptance for $\tau \rightarrow \mu ee$ for various observed particle combinations.

then subject to a fit which varies the three-particle energies so as to satisfy the beam energy constraint. These energies and the measured angles are then used to calculate the three-particle invariant mass M_3 .

There are many different sources which contribute background to this search, for example, electromagnetic events, hadronic events where pions are misidentified or decay to muons, converted photons in hadronic events, semileptonic decays of charmed particles, and τ events. Therefore, we use the following set of restrictions, which are discussed fully in Ref. 5.

(a) An event must not contain an electron pair from a converted photon.

(b) The average of the cosine of the coplanarity angle between a track and all other tracks in the event must be larger than -0.970 for all tracks. This eliminates most Bhabha-scattering events in which one of the electrons is accompanied by an electron pair.

The acceptances for the various modes range

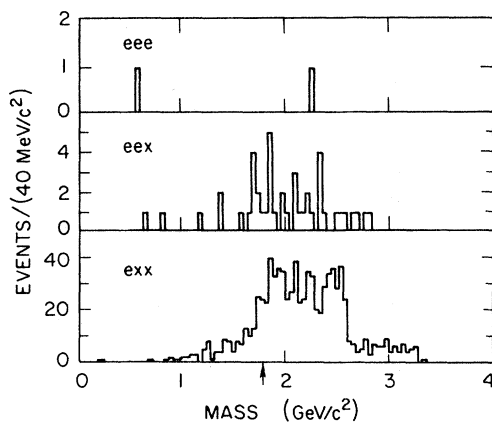


FIG. 12. The $e^\pm e^\pm e^\mp$ invariant-mass distributions. The arrow indicates the position of the τ mass $1.782 \text{ GeV}/c^2$.

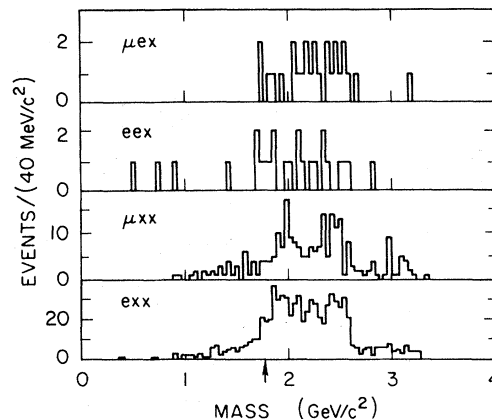


FIG. 13. The $\mu^\pm e^\pm e^\mp$ invariant-mass distributions. The arrow indicates the position of the τ mass $1.782 \text{ GeV}/c^2$.

from 0.01 to 0.20; Fig. 11 shows some examples.

The distributions for the invariant mass M_3 , for three-electron combinations with 1, 2, or 3 identified electrons, are shown in Fig. 12. There is no evidence in the plot for the decay $\tau \rightarrow eee$. Figures 13–15 show the equivalent plot for the other three decays: $\tau \rightarrow \mu ee$, $\tau \rightarrow e\mu\mu$, and $\tau \rightarrow \mu\mu\mu$. Again, no evidence can be seen for the decay of the τ to any three-charged-lepton combination.

Table III is a summary of the data for each of the four decays in this search. In this table we list, subdivided according to the category of identified leptons, the average acceptance for each decay, the number of detected events within the $40\text{-MeV}/c^2$ region used to define the acceptance, and the 90%-confidence-level upper limit on the branching ratio. Within any single decay, the results from different sets of identified lepton categories are sta-

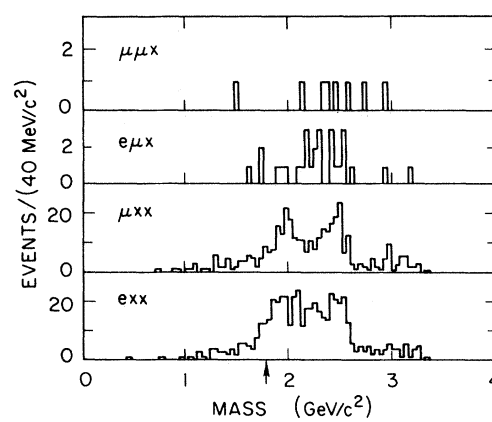


FIG. 14. The $e^\pm \mu^\pm \mu^\mp$ invariant-mass distributions. The arrow indicates the position of the τ mass $1.782 \text{ GeV}/c^2$.

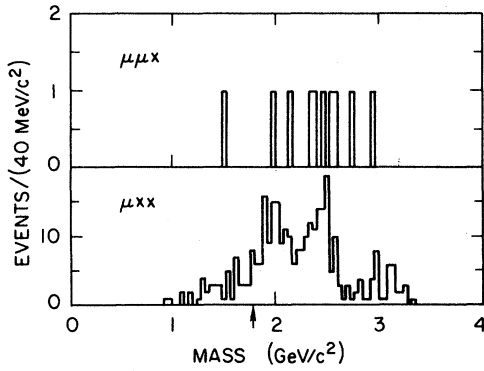


FIG. 15. The $\mu^\pm\mu^+\mu^-$ invariant-mass distributions. The arrow indicates the position of the τ mass $1.782 \text{ GeV}/c^2$.

tistically independent as different particle combinations contribute to each category. By adding the categories with the least background together, the overall limit on the branching ratios can be improved. Table IV summarizes the best limits obtainable in this way.

VI. SEARCH FOR DECAY OF THE τ TO A CHARGED LEPTON PLUS A NEUTRAL HADRON

In this section we describe the search for the decay modes

$$\tau^- \rightarrow e^- + \rho^0, \quad \tau^- \rightarrow \mu^- + \rho^0, \quad (21)$$

$$\tau^- \rightarrow e^- + K^0, \quad \tau^- \rightarrow \mu^- + K^0, \quad (22)$$

$$\tau^- \rightarrow e^- + \pi^0, \quad \tau^- \rightarrow \mu^- + \pi^0. \quad (23)$$

Although these are two-body decays, the hadrons are short-lived and can be measured only by detecting their decay products. The ρ^0 is reconstructed from its $\pi^+\pi^-$ decay. As its large width allows only a loose mass cut to be made, the analysis is very similar to that of the three-charged-lepton decays discussed in Sec. V. The K^0 is reconstructed from the $\pi^+\pi^-$ decay mode of its short-lived component. The fact that the K^0 can travel an appreciable distance from the interaction region before decaying, and the kinematic constraint provided by its narrow width requires a more detailed analysis to be made but results in an improved signal-to-background ratio relative to the ρ -lepton decay. Photons detected in the liquid-argon shower detector are used to reconstruct the π^0 . The shower-counter detection efficiency and limited solid angle restrict the acceptance, resulting in a reduced sensitivity for the $l^\pm + \pi^0$ decay mode search.

The data sample, containing 48 000 produced τ pairs, is the same used in the previous analyses. The event topology used in the $l^\pm + \rho^0$ and $l^\pm + K^0$ search is the same as that used in the three-

TABLE III. 90%-confidence-level upper limit on $\tau \rightarrow$ three-charged-lepton decays.

Decay	Type	Average acceptance(%)	Number detected events	Branching-ratio upper limit(%)
$\mu\mu\mu$	$\mu x x$	15.7	8	0.086
	$\mu\mu x$	4.6	0	0.052
	$\mu\mu\mu$	0.28	0	0.86
$e\mu\mu$	$\mu x x$	5.4	9	0.28
	$e x x$	7.1	13	0.28
	$\mu\mu x$	0.87	0	0.28
	$e\mu x$	5.8	0	0.042
	$e\mu\mu$	0.68	0	0.35
$\mu e e$	$\mu x x$	1.5	4	0.56
	$e x x$	7.1	13	0.38
	$\mu e x$	3.4	0	0.070
	$e e x$	4.2	1	0.10
	$\mu e e$	1.7	0	0.14
$e e e$	$e x x$	5.8	24	0.57
	$e e x$	7.3	1	0.056
	$e e e$	2.8	0	0.086

TABLE IV. 90%-confidence-level upper limits on τ decay modes. The detector acceptance for each mode is given in column 3, and the number of events found within the τ mass resolution is given in column 4. The limits include the charge-conjugate decay modes.

Decay mode $\tau^- \rightarrow$	Upper limit on branching fraction	Acceptance(%)	No. of events found at τ mass
$\mu^- + \gamma$	5.5×10^{-4}	7.3	1
$e^- + \gamma$	6.4×10^{-4}	6.3	1
$\mu^- + \mu^+ + \mu^-$	4.9×10^{-4}	4.9	0
$e^- + \mu^+ + \mu^-$	3.3×10^{-4}	7.3	0
$\mu^- + e^+ + e^-$	4.4×10^{-4}	9.3	1
$e^- + e^+ + e^-$	4.0×10^{-4}	10.1	1
$\mu^- + \pi^0$	8.2×10^{-4}	2.9	0
$e^- + \pi^0$	21.0×10^{-4}	3.5	3
$\mu^- + K^0$	10.0×10^{-4}	2.4	0
$e^- + K^0$	13.0×10^{-4}	3.1	1
$\mu^- + \rho^0$	4.4×10^{-4}	5.5	0
$e^- + \rho^0$	3.7×10^{-4}	6.5	0

charged-lepton decay search (except for one vertex cut in the K^0 analysis), while the topology used in the $l^\pm + \pi^0$ search is the same as that used in the $l^\pm + \gamma$ search except that we require at least two photons to be detected in the event. Other similarities exist between this analysis and the previous ones, and we shall make many references to material previously presented.

The remainder of this section is divided into three parts. First we will discuss the search for the $l^\pm + \rho^0$ decay of the τ , followed by $l^\pm + K^0$ and $l^\pm + \pi^0$ searches.

A. Search for $l^\pm + \rho^0$

The search for $l^\pm + \rho^0$ is very similar to the three-charged-lepton analysis discussed in Sec. V for the μ_{xx} and e_{xx} identification categories. There are only three differences.

(a) The two x tracks are assumed to be pions and must have opposite charge.

(b) To reduce the background a tighter cut is applied on the measured total energy of the three tracks. Defining

$$Z = (E_l + E_{\pi^+} + E_{\pi^-}) / E_{\text{beam}} \quad (24)$$

and

$$y = (E_{\text{c.m.}} - 4.0) \text{ GeV}, \quad (25)$$

we require

$$\mu + \rho: 0.975(1 - 0.0038y)$$

$$< Z < 1.025(1 + 0.0038y),$$

$$e + \rho: 0.975(1 - 0.0038y)$$

$$< Z < 1.020(1 + 0.0038y). \quad (26)$$

As the resolution in Z changes with the beam energy, the cut is now made to vary with the total energy. (In the analysis of the three-lepton decay modes, the resolution in Z also changes with energy, but the background was smaller there and we could use a simpler, fixed Z cut.)

(c) The invariant mass of the two pions must be consistent with the ρ^0 mass. In Fig. 16 we plot the measured two-pion invariant-mass distribution for all $\mu^-(\pi^+\pi^-)$ candidate events passing the total energy (Z) cut compared to the Breit-Wigner distribution expected for the ρ . A small ρ signal is seen, and to maximize the signal-to-background ratio, the $\pi^+\pi^-$ invariant mass is required to be within

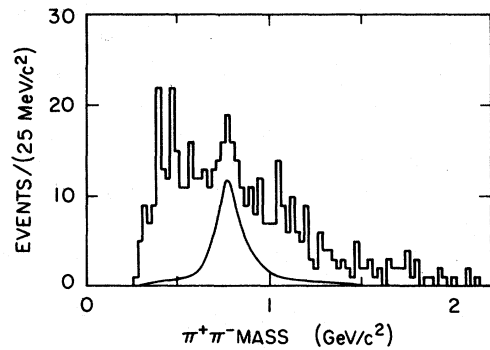


FIG. 16. The $\pi^+\pi^-$ invariant mass for $\mu^-(\pi^+\pi^-)$ candidates. The curve is a Breit-Wigner distribution for the ρ^0 .

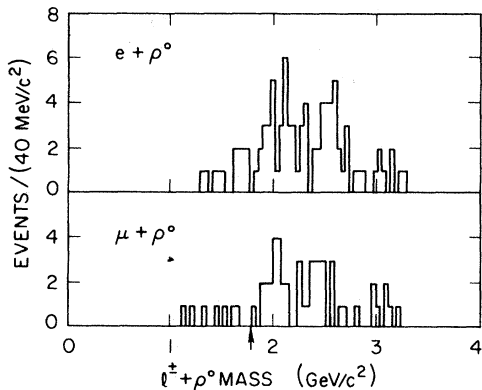


FIG. 17. The $l+\rho^0$ invariant-mass distributions. The arrow indicates the position of the τ mass $1.782 \text{ GeV}/c^2$.

$100 \text{ MeV}/c^2$ of the ρ mass.

The beam-constrained $l^\pm+\rho^0$ mass distributions obtained after applying the above cuts are shown in Figs. 17 and 18 for the μ - ρ and e - ρ candidates. We see no evidence for the decays $\tau\rightarrow\mu+\rho$ or $\tau\rightarrow e+\rho$.

The acceptance using those events within $20 \text{ MeV}/c^2$ of the τ mass is 5.5% for the $\tau\rightarrow\mu+\rho$ and 6.5% for the $\tau\rightarrow e+\rho$ decay. Given that no μ - ρ events are detected within the acceptance window, the 90%-confidence-level upper limit on the branching ratio for the decay $\tau\rightarrow\mu+\rho$ is 0.044%. There are also no e - ρ events detected within the acceptance window. The 90%-C.L. upper limit on the branching fraction for the decay $\tau\rightarrow e+\rho$ is 0.037%.

B. Search for $l^\pm+K^0$

The search for $l^\pm+K^0$ is somewhat more involved than the search for $l^\pm+\rho^0$. Since we only use the decay mode $K_S^0\rightarrow\pi^+\pi^-$, the net acceptance will be reduced by a factor of 0.34. However, the fact that the kaon decay vertex is most often located away from the primary vertex can be used to significantly reduce the background. But we can no longer demand that the two pion tracks originate in the primary vertex. All the other vertex, topological, and background-removing cuts used in the three-charged-lepton τ -decay search are retained.

The K^0 reconstruction algorithm is straightforward and yields a relatively clean kaon sample. We exploit the fact that in the uniform magnetic field of the Mark II, the charged-particle trajectories projected in the xy plane are circles. The de-

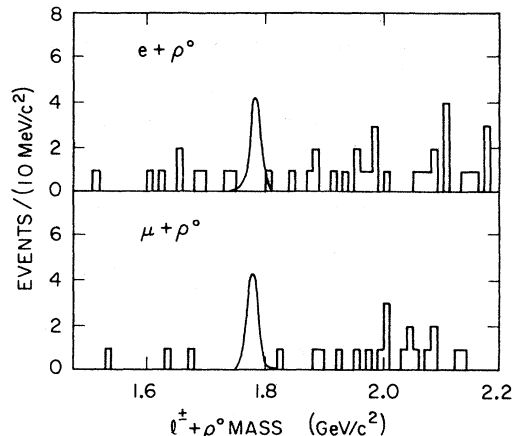


FIG. 18. The $l+\rho^0$ invariant-mass distributions in the neighborhood of the τ mass. The mass-resolution-function curve is centered on the τ mass $1.782 \text{ GeV}/c^2$.

decay vertex is located at one of the two points where the circles intersect, and the invariant mass of the two tracks, calculated with the momenta measured at the decay vertex (not the point of closest approach to the interaction region) is—within errors—the K^0 mass. The algorithm is described in detail in Ref. 5. Figure 19 shows the dipion invariant-mass distribution from a sample of multiprong as well as two-prong events. The K^0 mass resolution is $\sigma\approx 6 \text{ MeV}/c^2$. Only those pairs with a mass within $18 \text{ MeV}/c^2$ of the kaon mass are retained.

We now address the question of the kinematic constraints which exist for this decay mode. We use Z and y as defined in Eqs. (24) and (25). The beam-energy constraint applies as before although the Z restriction must be made looser because the momentum resolution is degraded for tracks which do not originate near the interaction region. We use

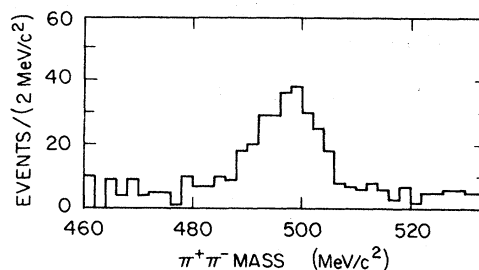


FIG. 19. The $\pi^+\pi^-$ invariant-mass distribution for $l+K^0$ candidate events.

$$\begin{aligned} \mu + K^0: & 0.960(1 - 0.0077y) \\ & < Z < 1.040(1 + 0.0077y) , \end{aligned} \quad (27)$$

$$\begin{aligned} e + K^0: & 0.950(1 - 0.0077y) \\ & < Z < 1.040(1 + 0.0077y) . \end{aligned}$$

These cuts were determined using the Monte Carlo simulation program and are looser than the $l^\pm + \rho^0$ cuts both because the resolution is poorer and the background is much reduced due to the K^0 requirement.

For those candidates which pass the Z cut, we apply the beam-constraint technique to improve the $l^\pm + K^0$ mass resolution. This yields a mass resolution $\sigma \approx 8.7 \text{ MeV}/c^2$.

The $\mu + K^0$ and $e + K^0$ mass distributions are shown in Fig. 20. The distributions contain no evidence for these decay modes of the τ . The acceptance is 2.4% for the $\mu + K^0$ decay and 3.1% for the $e + K^0$ decay of the τ . Given that no $\mu + K^0$ events are observed which have an invariant mass within $20 \text{ MeV}/c^2$ of the τ mass, we can set a 90%-confidence-level upper limit on the branching fraction for the decay $\tau \rightarrow \mu + K^0$ of 0.10%. The single $e + K^0$ event observed in the 40-MeV/ c^2 acceptance window determines the 90%-C.L. upper limit on the branching fraction for the decay $\tau \rightarrow e + K^0$ of 0.13%.

C. Search for $l + \pi^0$

The final charged lepton + neutral hadron τ decays we shall discuss are the $\tau \rightarrow \mu + \pi^0$ and

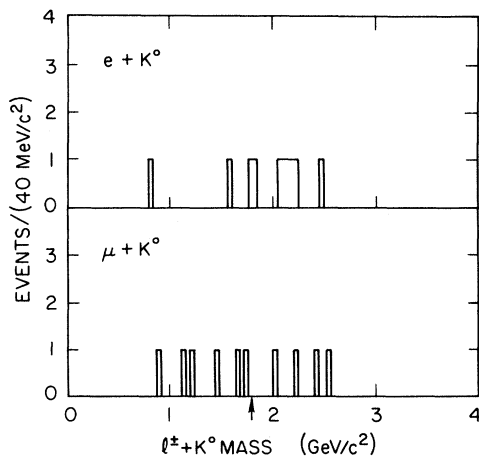


FIG. 20. The $l + K^0$ invariant-mass distributions. The arrow indicates the position of the τ mass $1.782 \text{ GeV}/c^2$.

$\tau \rightarrow e + \pi^0$ decays. This analysis is in many ways similar to that of the search for the $l + \gamma$ decays discussed in Sec. IV. A subset of the events used in that analysis is used here: two oppositely charged, acoplanar tracks which originate in the interaction region, one or more of which is identified as a lepton, with two or more photons detected in the liquid-argon shower detector. Therefore, there are the same sources of background. The restrictions discussed in Sec. IV to eliminate events of purely electromagnetic origin are also used in this analysis as they have a negligible effect on the acceptance, less than 2%, but reduce the background significantly. Because the $l + \pi^0$ mass resolution is dominated by the photon energy resolution, the beam-constraint technique yields nearly the same mass resolution as existed in the radiative decay search, and the inclusion of the pion mass constraint improves this somewhat. The acceptance is significantly smaller, however, as the two photons from the decay must be detected, and the sensitivity of this search is correspondingly reduced.

The π^0 reconstruction algorithm is simple: all photon pairs whose invariant mass is consistent with the neutral-pion mass are called π^0 's. No attempt is made to resolve the ambiguity if a photon is used in more than one π^0 . The π^0 mass resolution (Fig. 21) depends upon the π^0 energy and the π^0 decay asymmetry parameter

$$a = 0.5 - \frac{|E_1 - E_2|}{2(E_1 + E_2)} . \quad (28)$$

Here E_1 and E_2 are the energies of the γ 's.

Two major cuts are used to decide whether a

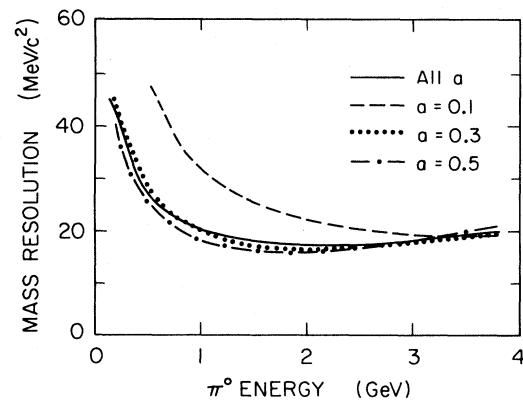


FIG. 21. The calculated π^0 mass resolution σ for various values of the asymmetry parameter a , defined in Eq. (28).

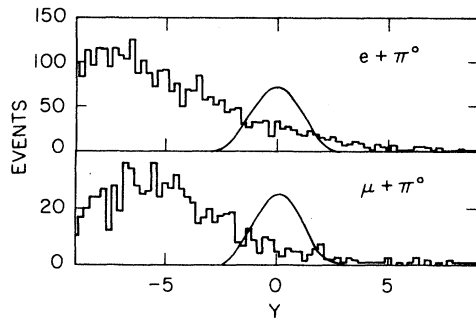


FIG. 22. The $Y = (E_l + E_{\pi^0} - E_{\text{beam}}) / \sigma(E_l + E_{\pi^0})$ distribution for $l + \pi^0$ candidates. The curve is the calculated distribution for the $\tau \rightarrow l + \pi^0$.

given photon pair is to be called a π^0 . The pair is required to have an invariant mass between 50 and 250 MeV/c^2 . Pairs which survive this cut are subject to a 1C fit to the π^0 mass in which all the photon parameters are varied, and those which have a χ^2 less than 5 are called π^0 s. These cuts are loose and maximize the π^0 detection efficiency at the expense of a large background.

Having reconstructed the π^0 s, the invariant mass is calculated for all $l^\pm + \pi^0$ combinations which have a total energy consistent with the beam energy. As the resolution in $E_{\text{tot}} = E_l + E_{\pi^0}$ varies with the lepton and pion energy, a cut is applied to the normalized variable

$$Y = (E_{\text{tot}} - E_{\text{beam}}) / \sigma(E_{\text{tot}}), \quad (29)$$

where $\sigma(E_{\text{tot}})$ is the σ for E_{tot} . Y^2 is equal to the χ^2 for the 1C fit constraining E_{tot} to the beam energy. Figure 22 shows the measured Y distribution for both the $e + \pi^0$ and $\mu + \pi^0$ candidates along with the expected distributions for $l + \pi^0$ τ decays calculated with the Monte Carlo simulation program. All combinations for which the magnitude of Y is greater than 2 are rejected.

The $l + \pi^0$ mass resolution varies with the asymmetry of the decay, and deteriorates rapidly as the lepton energy approaches the beam energy. Hence we reject events with $E_l/E_{\text{beam}} > 0.8$.

Figure 23 shows the constrained $l + \pi^0$ mass for all candidates passing the decay constraints. A large background is present which originates from several sources, and the following restrictions⁵ are used to suppress it.

(a) The π^0 must not contain a photon coming from an electron bremsstrahlung.

(b) Each photon in the π^0 must have greater than 200 MeV energy. This removes background due to false photons created by noise in the

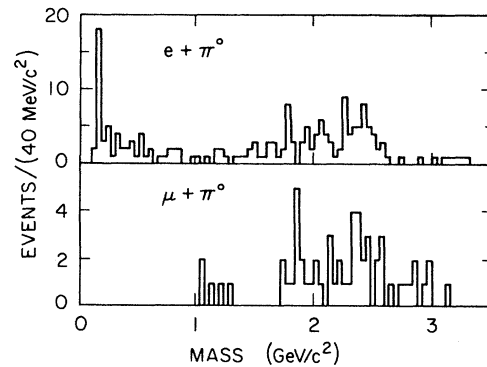


FIG. 23. The $l + \pi^0$ invariant-mass distributions before the application of background-reducing constraints.

shower-detector electronics.

(c) The a of the π^0 , Eq. (28), must be greater than 0.15. This reduces the background in π^0 s of moderate to high energy due to the incorrect but statistically preferred pairing of one low-energy and one high-energy background photon.

(d) The acoplanarity angle⁹ must be greater than 12° .

(e) The invariant mass of the π^0 and of the non- l charged particle must *not* lie in the ρ^0 mass region of 650 to 950 MeV/c^2 . This eliminates background from τ -pair decays which contain $\tau^\pm \rightarrow \rho^\pm + \nu$.

Figure 24 shows the $l + \pi^0$ mass distributions with these constraints. No evidence is seen for the $\mu + \pi^0$ decay of the τ . The acceptance is 2.9%. No events are detected within the 40-MeV/ c^2 region which defines the acceptance. This determines the 90%-confidence-level upper limit to the branching fraction for $\tau \rightarrow \mu + \pi^0$ to be 0.082%.

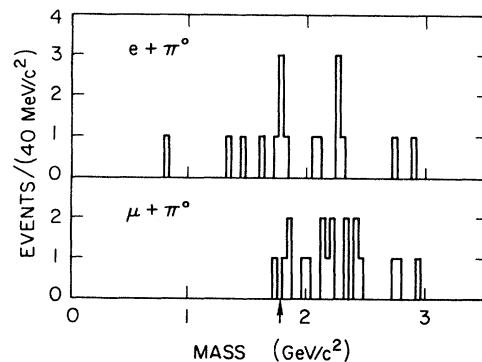


FIG. 24. The $l + \pi^0$ invariant-mass distributions after the application of background-reducing constraints. The arrow indicates the position of the τ mass 1.782 GeV/c^2 .

Finally we turn to the search for $\tau \rightarrow e + \pi^0$. Application of all constraints discussed above, three events remain in the 40-MeV/c²-wide bin encompassing the τ mass. The acceptance is 3.5%. The 90%-confidence-level upper limit on the branching fraction for the decay $\tau \rightarrow e + \pi^0$ is 0.21%.

VII. SEARCH FOR UNCONVENTIONAL PAIR-PRODUCED PARTICLES

In the analyses described in Secs. IV–VI, we did not require that the particle have the τ mass until the acceptance was calculated. Hence the mass spectra in Figs. 9, 12–15, 17, 20, and 23 apply to any pair-produced particle x^\pm with the indicated decay mode. Since the spectra extend from less than 1 GeV/c² to above 3 GeV/c² these figures summarize a general search for particles in this mass range produced via

$$e^+ + e^- \rightarrow x^+ + x^- . \quad (30)$$

The bin width in the figures is 25 or 40 MeV/c², and the σ of the expected mass resolution is 8 to 30 MeV/c². A new particle would be indicated by a peak of *substantial* statistical significance with a width of up to several bins. We do not observe such a peak in any of these spectra.

A great deal of work is required to convert this qualitative observation to quantitative upper limits on the products of production cross sections and branching fractions. Monte Carlo methods must be used to calculate the acceptance and mass resolution at all masses of interest. Furthermore, one must assume a knowledge of all the decay modes

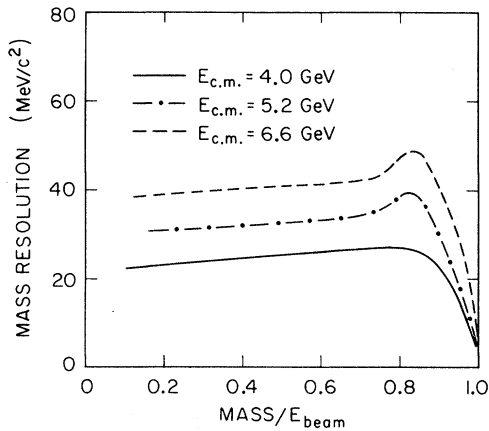


FIG. 25. The width of the mass resolution function containing 80% of the detected events for $\mu^* \rightarrow \mu + \gamma$ as a function of $\text{mass}_{\mu^*}/E_{\text{beam}}$.

in order to calculate the probability of the x^+x^- pair fitting the basic event signature of Eq. (8).

We felt that it was worthwhile to carry out such calculations for hypothetical excited leptons.¹⁰ We studied two types. The μ^* has only one decay mode

$$\mu^{*\pm} \rightarrow \mu^\pm + \gamma \quad (31a)$$

and is produced via

$$e^+ + e^- \rightarrow \mu^{*+} + \mu^{*-} . \quad (31b)$$

We have not considered

$$e^+ + e^- \rightarrow \mu^{*\pm} + \mu^\mp .$$

Analogously we considered

$$e^{*\pm} \rightarrow e^\pm + \gamma \quad (32a)$$

produced via

$$e^+ + e^- \rightarrow e^{*+} + e^{*-} . \quad (32b)$$

Pioneering searches for the e^* were carried out at the ADONE e^+e^- colliding-beams facility.¹¹

A. Search for $\mu^* \rightarrow \mu + \gamma$

We assume

$$\sigma(ee \rightarrow \mu^* \mu^*) = R_{\mu^*} \frac{2\pi\alpha^2\beta(3-\beta^2)}{3E_{\text{c.m.}}^2} , \quad (33)$$

where β is the lepton velocity in units of c and α is the fine-structure constant. We use Fig. 9(b) to calculate upper limits on R_{μ^*} . Figures 25 and 26 show, respectively, the μ^* mass resolution and the acceptance for detecting the decay $\mu^* \rightarrow \mu + \gamma$. Figure 27 gives the number of $\mu^* \rightarrow \mu + \gamma$ which would have been detected if $R_{\mu^*} = 1$. For masses between

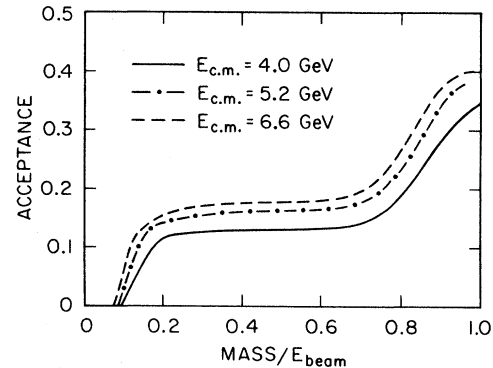


FIG. 26. The acceptance for $\mu^* \rightarrow \mu + \gamma$ as a function of $\text{mass}_{\mu^*}/E_{\text{beam}}$.

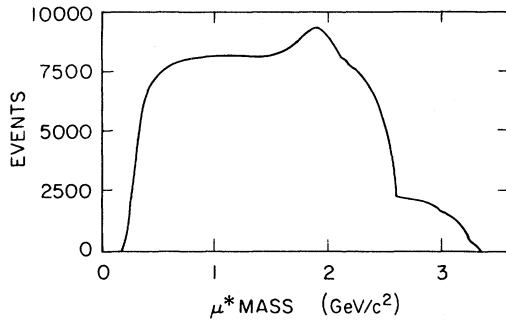


FIG. 27. Number of $\mu^* \rightarrow \mu + \gamma$ events which would have been detected if $R(e^+e^- \rightarrow \mu^* + \mu^{*-}) = 1$ versus the μ^* mass.

0.6 and 2.2 GeV/c^2 we would expect to detect approximately 8000 μ^* 's if they were produced with the point cross section and decayed with unit branching fraction to the $\mu + \gamma$ final state. For masses below 0.5 GeV/c^2 , the decreasing acceptance limits this while above 2.6 GeV/c^2 only the high-energy data contribute. The steep shoulder between 2.2 and 2.6 GeV/c^2 is a reflection of the threshold function in the cross section and the large fraction of data with $E_{\text{c.m.}} = 5.2 \text{ GeV}$.

Using Figs. 9(b) and 27 we can determine an upper limit for the cross-section suppression factor R_{μ^*} . In Table V we list, for various mass intervals, 90%-confidence-level upper limits on R_{μ^*} . These are the worst case values obtained by dividing the 90% Poisson probability for the largest sum of three adjacent bins within the mass interval by the minimum expected number of detected events. Within these intervals there are certain regions where the limits are considerably better than the worst case values, but never better than 0.0004.

B. Search for $e^* \rightarrow e + \gamma$

We determine upper limits on R_{e^*} for e^* 's produced via $e^+ + e^- \rightarrow e^{*+} + e^{*-}$ in exactly the same

TABLE V. 90%-confidence-level upper limit on R_{μ^*} .

Mass interval (GeV/c^2)	Maximum bin sum	90%-confidence-level upper limit on R_{μ^*}
0.6–1.6	3	0.0010
1.6–2.1	5	0.0014
2.1–2.5	6	0.0025
2.5–2.9	3	0.0043
2.9–3.2	3	0.0090
3.2–3.3	1	0.0193

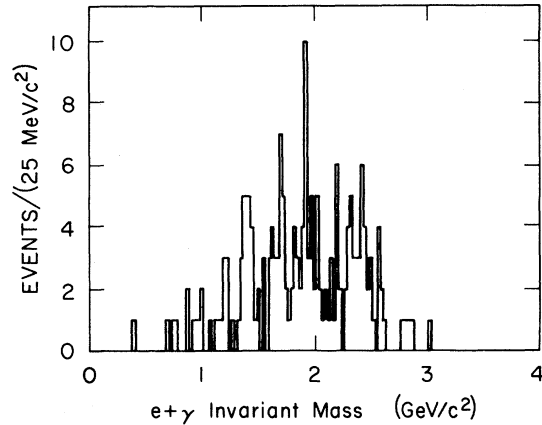


FIG. 28. The $e\text{-}\gamma$ invariant-mass distribution for $e^+ + e^- \rightarrow e^{*+} + e^{*-}$ candidates.

way that upper limits on R_{μ^*} were set. Here

$$\sigma(ee \rightarrow e^*e^*) = R_{e^*} \frac{2\pi\alpha^2\beta(3-\beta^2)}{3E_{\text{c.m.}}^2}. \quad (34)$$

However, the condition used to search for $\tau \rightarrow e + \gamma$ in Sec. IV, that the track opposite to the $e + \gamma$ not be an electron, cannot be used. This leads to the $e + \gamma$ mass distribution shown in Fig. 28. The expected number of detected $e + \gamma$ events (shown as a function of the e^* mass in Fig. 29) is less than the μ^* case due to the tighter acoplanarity cut. Table VI lists the resulting 90%-confidence-level upper limits on R_{e^*} for various mass intervals.

Before concluding the paper we return to the question of whether significance should be attached to the existence in Fig. 10 of 5 $e\gamma$ mass pairs and 4 $\mu\gamma$ mass pairs in the vicinity of 1730 MeV/c^2 . Figure 10 shows a small mass range of Fig. 9. In

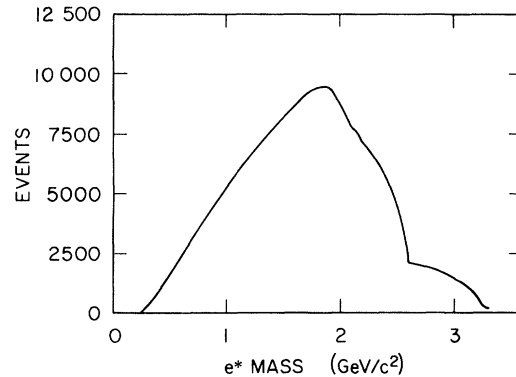


FIG. 29. Number of $e^* \rightarrow e + \gamma$ events which would have been detected if $R(e^+e^- \rightarrow e^* + e^{*-}) = 1$ versus the e^* mass.

Fig. 9 there are 70 $\mu\gamma$ mass pairs and 72 $e\gamma$ mass pairs. Our first task is to calculate the probability that these 9 pairs occur in the vicinity of 1730 MeV/c^2 by chance.

These 9 mass pairs occupy a mass range of 16 MeV/c^2 which makes their appearance so striking. However, as shown in Fig. 10 the width of the mass resolution curve at the τ mass is about 40 to 50 MeV/c^2 . Since this width varies slowly with the mass (Fig. 25), we will have similar resolution-curve widths at 1730 MeV/c^2 .

We can calculate the probability of obtaining by chance this combination of 9 pairs in a 16- MeV/c^2 width, and we do so below. However, we believe that a larger width should be used to give such a calculation physical significance. We choose that larger width as being 30 or 40 MeV/c^2 , since a reasonable fraction of the area of a resolution curve falls within that width. We define $P(W,9,4)$ as the total probability of finding two peaks within a range of W ; each peak having at least 4 pairs, and the total being at least 9 pairs. Assuming the backgrounds of Fig. 9 and Poisson statistics we find

$$\begin{aligned} P(16 \text{ MeV}/c^2, 9, 4) &= 0.0013, \\ P(30 \text{ MeV}/c^2, 9, 4) &= 0.065, \\ P(40 \text{ MeV}/c^2, 9, 4) &= 0.30. \end{aligned} \quad (35)$$

The coincidence of the peaks in Fig. 10 would still be apparent if each of the peaks had at least 3 pairs and the total was at least 9. Therefore, we also consider the larger probabilities

$$\begin{aligned} P(16 \text{ MeV}/c^2, 9, 3) &= 0.0021, \\ P(30 \text{ MeV}/c^2, 9, 3) &= 0.10, \\ P(40 \text{ MeV}/c^2, 9, 3) &= 0.42. \end{aligned} \quad (36)$$

TABLE VI. 90%-confidence-level upper limit on R_{e^*} .

Mass interval (GeV/c^2)	Maximum bin sum	90%-confidence-level upper limit on R_{e^*}
0.5–0.6	0	0.0014
0.6–0.8	3	0.0027
0.8–1.0	5	0.0023
1.0–1.3	8	0.0025
1.3–2.0	22	0.0041
2.0–2.3	15	0.0030
2.3–2.5	16	0.0051
2.5–3.0	10	0.0096
3.0–3.2	1	0.0039
3.2–3.3	0	0.0110

There are two comments to be made on the probabilities given in Eqs. (35) and (36). First, 8 of the 9 mass pairs come from events with $3.85 < E_{c.m.} < 4.45 \text{ GeV}$. As shown in Table II, this energy range constitutes about one quarter of the data. If we use this energy range there is less background and the probabilities are smaller. Specifically for $3.85 < E_{c.m.} < 4.45 \text{ GeV}$,

$$\begin{aligned} P(16 \text{ MeV}/c^2, 8, 3) &= 0.00047, \\ P(30 \text{ MeV}/c^2, 8, 3) &= 0.011, \\ P(40 \text{ MeV}/c^2, 8, 3) &= 0.040. \end{aligned} \quad (37)$$

However, since this $E_{c.m.}$ criteria was set *after* looking at the data, this is a dangerous way to reduce these probabilities.

The second comment is that our method of calculating the probabilities underestimates them. The method assumes that the positions of the bins on the mass scale are fixed, and then the probability of obtaining the desired peaks in any of these fixed bins is calculated. The method does not allow for sliding the bins along the mass scale to enhance the peaks in a particular pair of bins. But that is what the eye does in picking out the coincidence of peaks in Fig. 10. We have not corrected the probabilities upward for this effect because the unevenness of the background makes such a correction unreliable.

The probabilities in Eqs. (35)–(37) are not small enough to demand a nonrandom explanation of the coincidence of peaks in Fig. 10. An example of a nonrandom explanation would be a mass 1730 MeV/c^2 particle with $e\gamma$ and $\mu\gamma$ decay modes. And even this explanation does not explain the abnormally narrow width of the peaks. Therefore, we conclude that this is a random effect in our data.

VIII. SUMMARY

Table IV summarizes the 90%-confidence upper limits on the branching fractions. We have also given the detection efficiency for each decay mode and the number of events found at the τ mass.

We have not found any decay modes of the τ which violate the concept that the τ and its associated neutrino have a unique, conserved lepton number. This agrees, as do all other published results, with the τ being a sequential lepton.

The upper limits in Table IV are factors of 10 or

more smaller than previously measured upper limits.¹² This improvement comes chiefly from the large data sample. Since it is difficult to increase the detector acceptances by more than a factor of 2 or 3, any substantial reduction in these upper limits will require the acquisition of a yet larger data sample.

We have not found any evidence for the ex-

istence of leptons which decay via $e^* \rightarrow e + \gamma$ or $\mu^* \rightarrow \mu + \gamma$ up to a mass of $3.3 \text{ GeV}/c^2$.

ACKNOWLEDGMENT

This work was supported by the U. S. Department of Energy under Contracts Nos. DE-AC03-76SF00515 and W-7405-ENG-48.

*Present address: CERN, Geneva, Switzerland.

†Present address: Vanderbilt University, Nashville, Tennessee 37235.

‡Present address: California Institute of Technology, Pasadena, California 91125.

§Present address: Harvard University, Cambridge, Massachusetts 02138.

|| Present address: Universität Bonn, D-53 Bonn, Federal Republic of Germany.

¶Present address: Centre d'Etudes Nucléaires de Saclay, F-91190 Gif-sur-Yvette, France.

**Present address: DESY, Hamburg, Germany.

¹M. L. Perl, *Ann. Rev. Nucl. Part. Sci.* **30**, 299 (1980).

²G. Flugge, *Z. Phys. C* **1**, 121 (1979).

³Y. S. Tsai, *Phys. Rev. D* **4**, 2821 (1971).

⁴H. B. Thacker and J. J. Sakurai, *Phys. Lett.* **B36**, 103 (1971).

⁵K. G. Hayes, Ph.D. Thesis, SLAC Report No. 237, 1981 (unpublished).

⁶R. H. Schindler, Ph.D. Thesis, SLAC Report No. 219, 1979 (unpublished).

⁷G. S. Abrams *et al.*, *IEEE Trans. Nucl. Sci.* **NS-27**, 59 (1980).

⁸T. M. Himel, Ph.D. Thesis, SLAC Report No. 223, 1979 (unpublished).

⁹The acoplanarity angle is defined by

$$\text{arc cos} \frac{(\vec{u}_1 \times \vec{u}_b) \cdot (\vec{u}_2 \times \vec{u}_b)}{|\vec{u}_1 \times \vec{u}_b| |\vec{u}_2 \times \vec{u}_b|},$$

where u_1, u_2, u_b are unit vectors in the direction of each of the final particles and of the beam, respectively.

¹⁰For a recent reference see M. L. Perl, in *New Phenomena in Lepton-Hadron Physics*, edited by D. E. C. Fries and J. Wess (Plenum, New York, 1979), p. 115.

¹¹C. Bacci *et al.*, *Phys. Lett.* **71B**, 227 (1977); **44B**, 530 (1973).

¹²M. L. Perl, in *Proceedings of the International Symposium on Lepton and Photon Interactions at High Energies, Hamburg, 1977*, edited by F. Gutbrod (DESY, Hamburg, 1977), p. 145.